Journal of Power Sources 185 (2008) 287–301

Contents lists available at ScienceDirect

Journal of Power Sources

journal homepage: www.elsevier.com/locate/jpowsour

A model for hydrogen sulfide poisoning in proton exchange membrane fuel cells

A.A. Shah*, F.C. Walsh

Energy Technology Research Group, School of Engineering Sciences, University of Southampton, University Road, Highfields, Southampton SO17 1BJ, United Kingdom

ARTICLE INFO

Article history:
Received 19 February 2008
Received in revised form 22 May 2008
Accepted 28 June 2008
Available online 10 July 2008

Keywords:
Degradation
Hydrogen sulfide poisoning
Mathematical model
PEM fuel cell
Simulation

ABSTRACT

A polymer-electrolyte fuel cell model that incorporates the effects of hydrogen sulfide contaminant on performance is developed. The model is transient, fully two-phase and non-isothermal and includes a complex kinetic mechanism to describe the electrode reactions. Comparisons between the simulation results and data in the literature demonstrate that known trends are well captured. The effects of temperature and relative humidity variations in the anode stream are investigated, with further comparisons to experimental data and a proposed explanation for the nonlinear behaviour observed in the experiments of Mohtadi et al. [R. Mohatadi, W.-K. Lee, J. van Zee, Appl. Catal. B 56 (2005) 37–42)]. Extensions to the model and future work are discussed.

1. Introduction

The proton exchange membrane (PEM) fuel cell has significant potential as an efficient and environmentally friendly power source. The main electrochemical reactions involve hydrogen and oxygen and in the absence of additional "side" reactions the net product is simply water. However, the main intended sources of hydrogen (H_2) are reformed hydrocarbons [2], which contain traces of ammonia, hydrogen sulfide and carbon monoxide. Each of these compounds engender reactions that seriously degrade performance and can potentially cause long-term harm to the positive electrode [3–5].

Carbon-monoxide (CO) poisoning has been studied quite extensively and the highly detrimental effects of small traces of CO in the anode fuel stream are well-documented [3,6,7]. Several mitigation techniques have been proposed and analysed, notably oxygen bleeding and the use of alternative catalysts such as platinum-ruthenium. The influence of hydrogen sulfide (H_2S), although first studied as early as 1971 by Loučka [4], is less well characterised. Several researchers have shown that small traces of H_2S severely affect performance, on a scale at least comparable with CO [1,4,8–18]. However, few mitigation strategies have been proposed and it has been reported that platinum-ruthenium, while effective against CO, is not H_2S tolerant [13,15]. There is a clear need, therefore, for a better fundamental understanding and characterisation of the H_2S poisoning process.

Modelling and simulation are well-established tools in PEM fuel cell research, particularly with a focus on the effects of water retention in the cathode at steady state. The methodologies and techniques were recently reviewed in [19,20]. Examples of time-dependent models can be found in [21–23] and, in contrast to steady-state models, are relatively few in number, even though in potential dynamic applications such as automobile power, cell stacks rarely operate at steady state. Degradation mechanisms, moreover, are inherently transient, impacting performance on a long time scale, as in the case of carbon corrosion, or on a relatively short time scale, as with H_2S poisoning. Models of such mechanisms, to which one can add radical attack of the membrane and platinum dissolution and sintering, are rare. This is somewhat surprising considering that the commercial viability of PEM fuel cells is largely dependent upon overcoming or minimising degradation phenomena, many of which can potentially be simulated on a computer in a fraction of the time required for long-life experiments.

It is also important to note that degradation is typically influenced strongly by the properties of the cell components, by heat and mass transport, and by the operating conditions—this is certainly true of CO poisoning and membrane failure. In order to keep fitting parameters to a minimum and simulate operation over a broad range of conditions a model should ideally include these features explicitly. An earlier paper laid the foundations for a transient model of CO poisoning and oxygen bleeding on both platinum and platinum-ruthenium that explicitly incorporated the entire MEA, two-phase flow and temperature variations [24]. In this paper a similarly detailed model is developed to study the H_2S poisoning mechanism, using the results in [1,4,8–18] to derive a detailed sub-model for the anode kinetics.

* Corresponding author. Tel.: +44 23 8059 8520; fax: +44 23 8059 3131.
E-mail address: A.Shah@soton.ac.uk (A.A. Shah).

0378-7753/$ – see front matter © 2008 Elsevier B.V. All rights reserved.
doi:10.1016/j.jpowsour.2008.06.082

Nomenclature

A	specific surface area of agglomerates (m^{-1})
a	specific surface area of platinum (m^{-1})
a_w	water activity
c	molar concentration ($mol\,m^{-3}$)
C	specific heat capacity ($J\,kg^{-1}\,K^{-1}$)
d	mean pore diameter (m)
D	diffusion coefficient ($m^2\,s^{-1}$)
E	cell voltage (V)
E_0	open circuit voltage (V)
F	Faraday's constant ($C\,mol^{-1}$)
h	mass transfer coefficient (s^{-1})
H	Henry's constant
i	interaction parameter ($J\,mol^{-1}$)
j	current density ($A\,m^{-2}$)
$\mathcal{J}$	Leverette function
k	thermal conductivity ($W\,m^{-1}\,K^{-1}$)
L	thickness (m)
m	loading ($kg\,m^{-2}$)
M	molar mass ($kg\,mol^{-1}$)
N	agglomerate density (m^{-3})
p	liquid pressure (Pa)
p_g	gas pressure (Pa)
q	surface reaction rate ($mol\,m^{-2}\,s^{-1}$)
q_{O_2}	ORR rate ($mol\,m^{-3}\,s^{-1}$)
r	reaction rate constants (reaction dependent)
R	molar gas constant ($mol\,m^{-3}\,s^{-1}$)
R_{agg}	agglomerate radius (m)
s	saturation
S	source/sink ($mol\,m^{-3}\,s^{-1}$)
t	time (s)
T	temperature (K)
v	velocity ($m\,s^{-1}$)
x	mole fraction
y	distance (m or μm)

Greek letters

α	charge transfer coefficient
γ	diffusion rate through films (s^{-1})
δ	film thickness (m)
Δs	entropy ($J\,mol^{-1}\,K^{-1}$)
ϵ	volume fraction
η	overpotential (V)
θ	surface coverage
κ	absolute permeability (m^2)
λ	membrane water content
μ	dynamic viscosity ($kg\,m^{-1}\,s^{-1}$)
ν	fixed charge site concentration ($mol\,m^{-3}$)
ρ	density ($kg\,m^{-3}$)
σ'	surface tension ($N\,m^{-1}$)
σ	conductivity ($S\,m^{-1}$)
σ_i	collision diameter for species i (Å)
τ	molar area density ($mol\,m^{-2}$)
ϕ	potential (V)
χ	contact angle (deg)
Ω	collision integral (m^{-1})

Subscript

a	anode
agg	agglomerate
b	backward (reaction)
c	cathode
C	catalyst layer
cap	capillary
d	dissolved
e	electrolyte
g	gas
G	gas diffusion layer
f	forward (rate constants)
v	vapour
l	liquid
p	pore space
pt	platinum
ref	reference
s	solid/electronic
0	reference
$v \leftrightarrow l$	vapour to liquid
$v \leftrightarrow d$	vapour to dissolved
$d \leftrightarrow l$	dissolved to liquid

Superscript

l	equilibrium between liquid and dissolved phases
$*$	equilibrium between vapour and dissolved phases
$-$	boundary/initial value
$\widehat{\ }$	volume average

The next section describes the conservation equations and kinetic model. In Section 3 simulation results are presented, with a comparison to experimental data available in the literature. The effects of channel temperature and water activity variations on the poisoning process are then investigated, with further comparisons to experimental data from Mohtadi et al. [1]. A summary of the results and a discussion of future work are given in Section 4.

2. Model

In this section the main features of the model and the underlying assumptions are enumerated, followed by a description of the conservation principles, the kinetic model, the initial and boundary conditions and the numerical implementation. Details of the parameters and the fitting procedure are also provided.

1. **Domain**. The domain includes the entire MEA as depicted in Fig. 1. Each component is modelled explicitly. Where convenient the following notation is used: GDL for the Gas Diffusion Layer, CCL for the Cathode Catalyst Layer and ACL for the Anode Catalyst Layer.
2. **Catalyst layers**. The so-called "agglomerates model" is employed, in which the carbon support is assumed to form spherical clusters, surrounded by layers of electrolyte and liquid water. The pores between agglomerates are referred to as primary pores, distinct from the smaller pores between the carbon particles. Sufficient contact between the agglomerates to permit electron and proton migration is assumed.
3. **Reactant transport and transfer**. The reactants are considered to exist as species in both the gas and electrolyte phases. Deviations from Henry's law provide a driving force for interfacial mass transfer. Water exists in three forms: dissolved, vapour and liquid. Mass transfer is driven by deviations from an appropriate equilibrium.
4. **Water.** Water is considered to exist in three forms: as a dissolved species, as vapour and as liquid. It assumed that the *net* water produced is in liquid form. Condensation and evaporation are modelled using the approach in [25–27], and references therein,

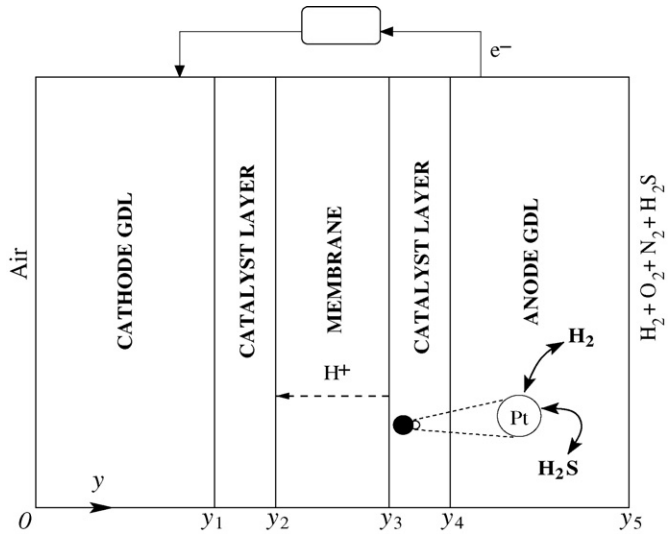

Fig. 1. A schematic of the one-dimensional domain considered in the model.

dictated by the deviation of the local thermodynamic state from equilibrium. In a similar fashion, phase change between vapour and dissolved water and between liquid and dissolved water are introduced by considering deviations from appropriate equilibrium states.

5. **Charge**. For the conservation of charge, electroneutrality and a pseudo steady-state apply. The justification can be found in [28].
6. **Kinetics**. The kinetics of oxygen reduction are assumed to follow a global mechanism, as is usually the case in modelling studies. The kinetic model at the anode is derived from the experimental results in [1,10–12,14].

2.1. Conservation principles

2.1.1. Reactant mass conservation

Let s denote liquid-water saturation, and c_i and $c^v_{H_2O}$ the pore concentrations of species $i = O_2$, H_2, N_2, H_2S, SO_3 and vapour, respectively. The concentration of species i dissolved in the electrolyte and membrane is denoted c^d_i. Mass balance equations in gas phase are derived by taking into account transport by diffusion and convection, and mass transfer to and from the electrolyte:

$$\frac{\partial}{\partial t}(\epsilon(1-s)c_i) - \frac{\partial}{\partial y}\left(D_i\frac{\partial c_i}{\partial y} - v_g c_i\right) = -S_{pi} \quad (1)$$

$$\frac{\partial}{\partial t}(\epsilon(1-s)c^v_{H_2O}) - \frac{\partial}{\partial y}\left(D^v_{H_2O}\frac{\partial c^v_{H_2O}}{\partial y} - v_g c^v_{H_2O}\right) = S_{v\leftrightarrow l} + \nu S_{v\leftrightarrow d} \quad (2)$$

where D_i is the free-space diffusion coefficient of species i in the pore space and $D^v_{H_2O}$ is the free-space diffusion coefficient for water vapour; T is temperature and p_g is the gas pressure; ϵ is the porosity, which takes the value $\epsilon = \epsilon_p$ in the catalyst layers and $\epsilon = \epsilon_G$ in the gas diffusion layers. The Chapman–Enskog approximation [29], and Bruggemann corrections have been used for the diffusion coefficients, with values referred to nitrogen:

$$D_i = 0.01858[\epsilon(1-s)]^{3/2}\frac{T^{3/2}}{p_g}\frac{\sqrt{(1/M_i)+(1/M_{N_2})}}{\sigma^2_{iN_2}\Omega_{iN_2}} \quad (3)$$

in $m^2\ s^{-1}$. For each species $i = M_i$ is the molar mass, σ_{iN_2} is the mean collision diameter (Lennard–Jones force constant) and Ω_{iN_2} is the collision integral. The vapour diffusion coefficient, $D^v_{H_2O}$, can be determined using the same formula. The collision diameters can be approximated by

$$\sigma_{N_2,i} = \frac{1}{2}(\sigma_i + \sigma_{N_2}),$$

where σ_i are the collision diameters for the individual species i. The values are given in Table 7 together with the collision integrals.

Table 1
Sources and sinks for the gas phase Eqs. (1)–(2)

Term	ACL	CCL	GDL
S_{pi}	$h_{pe,i}(H_i c_i - c^d_i)$	$h_{pe,i}(H_i c_i - c^d_i)$	0
$S_{v\leftrightarrow l}$	$-h_{v\leftrightarrow l}(x_v p_g - p_{sat})$	$-h_{v\leftrightarrow l}(x_v p_g - p_{sat})$	$-h_{v\leftrightarrow l}(x_v p_g - p_{sat})$
$S_{v\leftrightarrow d}$	$h_{v\leftrightarrow d}(c^d_{H_2O} - c^*_{H_2O})$	$h_{v\leftrightarrow d}(c^d_{H_2O} - c^*_{H_2O})$	0

These terms represent, from top to bottom, reactant dissolution in electrolyte, condensation/evaporation, and vapour/dissolved water mass transfer.

The gas velocity is given by Darcy's law for flow through a porous medium and the absolute permeability given by the Kozeny–Carman law:

$$v_g = -\frac{\kappa}{\mu}(1-s)^3\frac{\partial p_g}{\partial y}, \quad \kappa = \frac{d^2}{K}\frac{\epsilon^3}{(1-\epsilon)^2}, \quad (4)$$

where κ is the absolute permeability of the gas diffusion or catalyst layers, μ is the dynamic viscosity of the gas, d is a mean pore diameter and K is the Kozeny–Carman constant. The source terms are given in Table 1. S_{pi} is the rate of mass transfer between the electrolyte and gas phases, $S_{v\leftrightarrow l}$ is the rate of condensation/evaporation, and $S_{v\leftrightarrow d}$ is the rate of water mass transfer between the electrolyte and gas phases. In Table 1 $h_{pe,i}$ are volumetric mass-transfer coefficients from the gas to the membrane or electrolyte phase on the gas side and H_i are dimensionless Henry constants. Each $h_{pe,i}$ is approximated based on a local Sherwood number of 2 (for flow past a spherical particle [29]):

$$h_{pe,i} = \frac{aShD_i}{d} \geq O(10^5),$$

where a is the specific surface area of the agglomerates. The condensation/evaporation coefficient $h_{v\leftrightarrow l}$ is defined later. The quantity $\nu = 1800$ mol m^{-3} is the fixed-charge site concentration of the membrane,

The electrolyte volume fraction, ϵ_e, has two components: one from the films that coat the agglomerates (ϵ^f_e) and the other from the electrolyte contained in the agglomerate interiors (ϵ^i_e), with:

$$\epsilon_e = \epsilon^f_e + \epsilon^i_e.$$

To account for the volume change due to swelling, which is assumed to impact only the film thickness, the following relationship is used:

$$\epsilon^f_e = \epsilon^f_{e,0} + 0.0126\lambda,$$

where λ is the membrane water content (mol H_2O/mol SO_3^-) and $\epsilon^f_{e,0}$ represents the volume fraction of film without any swelling. The latter quantity is related to the film thickness without swelling, $\delta_{e,0}$, as shown in Table 6 and derived in [23]. The platinum inside the agglomerates is assumed to be inactive and therefore not to contribute to the electrochemical reaction. Thus all reaction occurs on the agglomerate surfaces. The combined volume fraction of the carbon, platinum and small pores, ϵ_a, is assumed constant. The volume fraction of primary pores is thus $\epsilon_p = 1 - \epsilon_a - \epsilon_e$.

Mass balance equations for species $i = O_2$, H_2, N_2, H_2S, SO_3dissolved in the electrolyte and membrane are derived by taking into account transport by diffusion, mass transfer to and from

Table 2
Sources and sinks for the dissolved reactants, potential and dissolved-water Eqs. (5), (13) and (6), respectively

	ACL	CCL	Meaning
S_{O_2}	0	$\frac{1}{4}q_{O_2}$	O_2 consumption
S_{H_2}	$a(-q_3+\frac{3}{2}q_2)$	0	H_2 consumption
S_{N_2}	0	0	N_2 consumption
S_{H_2S}	$-a(q_1+q_2+q_5)$	0	H_2S consumption
S_{SO_3}	aq_7	0	SO_3 production
S_e	$aF(q_4+2q_5+6q_7)$	Fq_{O_2}	Proton source
S_s	$-S_e$	$-S_e$	Electron source
$S_{d\leftrightarrow l}$	$h_{d\leftrightarrow l}(c^d_{H_2O}-c^l_{H_2O})$	$h_{d\leftrightarrow l}(c^d_{H_2O}-c^l_{H_2O})$	Liquid/dissolved water mass transfer
S_w	$-3aq_7$	$-\frac{1}{2}q_{O_2}$	Water production (liquid phase)

The last term represents liquid-water production in Eq. (8).

the gas phase, and consumption or generation by reaction:

$$\frac{\partial}{\partial t}(\epsilon c_i^d)-\frac{\partial}{\partial y}\left(\epsilon^{3/2}D_i^d\frac{\partial c_i^d}{\partial y}\right)=S_i+S_{pi}, \tag{5}$$

where $\epsilon=\epsilon_e$ in the catalyst layer, $\epsilon=1$ in the membrane and D_i^d are the free-space diffusion coefficients in the electrolyte used with Bruggeman corrections. The source terms S_i, $i=O_2$, H_2, N_2, H_2S, SO_3, are defined in Table 2 and are the rates of consumption or generation of species i. The surface reaction rates q and the volumetric reaction rate q_{O_2} will be defined in Section 2.2.

The mass balance for water dissolved in the electrolyte and membrane, normalised with respect to ν, $c^d_{H_2O}$, is derived by considering movement by diffusion and drag:

$$\frac{\partial}{\partial t}(\epsilon c^d_{H_2O})-\frac{\partial}{\partial y}\left(\epsilon^{3/2}D^d_{H_2O}\frac{\partial c^d_{H_2O}}{\partial y}+\frac{5\lambda}{44F\nu}\epsilon^{3/2}\sigma_e\frac{\partial\phi_e}{\partial y}\right)$$
$$=-S_{v\leftrightarrow d}-S_{d\leftrightarrow l}, \tag{6}$$

in which $\epsilon=1$ for the membrane and $\epsilon=\epsilon_e$ for the catalyst layer, and $D^d_{H_2O}$ is the diffusion coefficient of water in the electrolyte subject to a Bruggeman correction.

The following form of $D^d_{H_2O}$ for Nafion is taken from [30]:

$$D^d_{H_2O}=u_1\lambda(1+161\,e^{-\lambda})\exp\left(-\frac{2436}{T}\right),$$

where $u_1=4.17\times10^{-8}$ $m^2\,s^{-1}$. The source term $S_{v\leftrightarrow d}$ was previously defined and $S_{d\leftrightarrow l}$, given in Table 2, is the rate of water mass transfer between the liquid and dissolved phases. Both are discussed below. Note that the water content and concentration are related by

$$\lambda=\frac{c^d_{H_2O}}{u_2-0.0126c^d_{H_2O}}, \tag{7}$$

where $u_2=1\,mol\,m^{-3}$. Eq. (7) will be used in the sequel.

A mass balance of liquid water is derived considering transport by convection, driven by pressure gradients:

$$\frac{\epsilon\rho_l}{M_{H_2O}}\frac{\partial s}{\partial t}+\frac{\partial}{\partial y}\left(\frac{\epsilon\rho_l}{M_{H_2O}}v_l\right)=-S_{v\leftrightarrow l}+\nu S_{d\leftrightarrow l}+S_w, \tag{8}$$

where the liquid-water interstitial velocity v_l is given by Darcy's law:

$$v_l=-\frac{\kappa s^3}{\mu_l}\frac{\partial p}{\partial y}. \tag{9}$$

$\epsilon=\epsilon_G$ in the gas diffusion layers and $\epsilon=\epsilon_p$ in the catalyst layers. M_{H_2O}, μ_l and p are the molar mass, viscosity and pressure of the liquid water, respectively, and κ is the absolute permeability of the catalyst or gas diffusion layers. The factor of s^3 in Eq. (9) is the relative permeability. The source term S_w is defined in Table 2 and is the rate of liquid-water production.

By definition:

$$p=p_g-p_{cap}, \tag{10}$$

where p_{cap} is the capillary pressure. Combining Eqs. (8), (9) and (10) yields:

$$\frac{\epsilon\rho_l}{M_{H_2O}}\frac{\partial s}{\partial t}+\frac{\epsilon\kappa\rho_l}{\mu_l M_{H_2O}}\frac{\partial}{\partial y}\left(s^3\left(\frac{dp_{cap}}{ds}\frac{\partial s}{\partial y}-\frac{\partial p_g}{\partial y}\right)\right)$$
$$=-S_{v\leftrightarrow l}+\nu S_{d\leftrightarrow l}+S_w. \tag{11}$$

For a discussion on the form of the permeability and capillary pressure the reader is referred to [26]. In this paper the widely used Leverette function is adopted (found in, for example [31]):

$$p_{cap}=\sigma'\cos\chi_G\sqrt{\frac{\epsilon_G}{\kappa_G}}\mathcal{J}(1-s),$$
$$p_{cap}=\sigma'\cos\chi_C\sqrt{\frac{\epsilon_p}{\kappa_C}}\mathcal{J}(s), \tag{12}$$

for the gas diffusion and catalyst layers, respectively. In these expressions σ' is the surface tension and $\mathcal{J}(\xi)$ is the Leverette function:

$$\mathcal{J}(\xi)=1.417\xi-2.12\xi^2+1.262\xi^3$$

χ_C and κ_C are the contact angle and absolute permeability of the catalyst layers, respectively, and χ_G and κ_G are the contact angle and absolute permeability of the gas diffusion layers, respectively.

2.1.2. Charge conservation

Equations for the potentials in the electrolyte/membrane and carbon, ϕ_e and ϕ_s respectively, are derived from conservation of charge in each phase, assuming electroneutrality and steady-state conditions, as justified in the assumptions:

$$-\frac{\partial}{\partial y}\left(\epsilon^{3/2}\sigma_e\frac{\partial\phi_e}{\partial y}\right)-S_e=-\frac{\partial}{\partial y}\left(\epsilon^{3/2}\sigma_s\frac{\partial\phi_s}{\partial y}\right)+S_s=0, \tag{13}$$

where σ_e and σ_s are the protonic and electronic conductivity respectively, used with Bruggeman corrections, and F is Faraday's constant. $\epsilon=\epsilon_e$ in the catalyst layer and $\epsilon=1$ in the membrane for ϕ_e, while $\epsilon=1-\epsilon_G$ in the gas diffusion layer and $\epsilon=\epsilon_s$ in the catalyst layer for ϕ_s. The source terms S_s and S_e are defined in Table 2. The protonic conductivity is assumed to take the form given in [32] for Nafion:

$$\sigma_e=u_3\exp\left(\frac{1286}{303}-\frac{1286}{T}\right)(0.514\lambda-0.326), \tag{14}$$

where $u_3=1\,S\,m^{-1}$. The electronic conductivity is constant and its value is given in Table 10.

Table 3
Sources and sinks for the energy Eq. (15)

Term	Membrane	ACL	CCL	GDL
Q_{act}	0	$aF\eta_a q_4$	$F\eta_c q_{O_2}$	0
Q_{rev}	0	$-\Delta s_a T a q_4$	$\Delta s_c T q_{O_2}$	0
Q_{ohm}	$\sigma_e \left(\frac{\partial \phi_e}{\partial y}\right)^2$	$\sum_{j=e,s} \epsilon_j^{3/2} \sigma_j \left(\frac{\partial \phi_j}{\partial y}\right)^2$	$\sum_{j=e,s} \epsilon_j^{3/2} \sigma_j \left(\frac{\partial \phi_j}{\partial y}\right)^2$	$(1-\epsilon_G)^{3/2} \sigma_s \left(\frac{\partial \phi_s}{\partial y}\right)^2$
Q_{pc}	0	$-h_{gl} S_{v\leftrightarrow l}$	$-h_{gl} S_{v\leftrightarrow l}$	$-h_{gl} S_{v\leftrightarrow}$

They are, from top to bottom, activation losses, heats of reaction, ohmic losses and heats of evaporation.

2.1.3. Energy conservation

A thermal energy balance equation is derived by taking into account heat generation and heat transport through the gas, liquid and solid phases, and assuming a single temperature:

$$\frac{\partial}{\partial t}\left(\widehat{\rho C_p} T\right) + \frac{\partial}{\partial y}\left(\epsilon s \rho_l C_l v_l T + \epsilon(1-s)\rho_g C_g v_g T - \hat{k}\frac{\partial T}{\partial y}\right) = \sum_k Q_k, \tag{15}$$

in the catalyst and gas diffusion layers, and

$$\frac{\partial}{\partial t}\left(\rho_m C_m T\right) + \frac{\partial}{\partial y}\left(k_m \frac{\partial T}{\partial y}\right) = \sum_k Q_k, \tag{16}$$

in the membrane. In these equations ρ_l, ρ_g, ρ_m and ρ_s are the densities of the liquid, gas, membrane and solid phases, respectively, and C_l, C_g, C_m and C_s are the specific heat capacities of the liquid, gas, membrane and solid phases, respectively. $\hat{k}$ and $\widehat{\rho C_p}$ are the volume-averaged thermal conductivity and thermal capacitance:

$$\begin{aligned} \hat{k} &= k_p(1-s)\epsilon + k_l s\epsilon + k_s(1-\epsilon), \\ \widehat{\rho C_p} &= \epsilon s \rho_l C_l + \epsilon(1-s)\rho_g C_g + \rho_s C_s (1-\epsilon), \end{aligned} \tag{17}$$

where k_p, k_s and k_l are the thermal conductivities of the pore space, solid (averaged over carbon, electrolyte and platinum) and liquid water, respectively. In the gas diffusion layers $\epsilon = \epsilon_G$ and in the catalyst layers $\epsilon = \epsilon_p$. In the membrane the only form of heat transport is conduction. The gas phase thermal conductivity and specific heat capacity are approximated by values for air. The heat generation terms Q_k are defined in Table 3. In these expressions h_{gl} is the liquid–gas enthalpy change for water, $-\Delta s_c$ is the entropy associated with the oxygen reduction reaction and $-\Delta s_a$ is the entropy associated with the hydrogen oxidation reaction. Note that as a simplification, the heats of reaction of the other anode reactions are neglected.

2.1.4. Water phase change

The treatment of water mass transfer between the three phases is now detailed. Condensation and evaporation are driven by the deviation from equilibrium: $x_v p_g - p_{sat}$, where p_{sat} is the saturation pressure of water and the first term, in which x_v is the vapour mole fraction, is the partial pressure of the vapour. The condensation/evaporation coefficient $h_{v\leftrightarrow l}$ in Table 1 takes the form:

$$h_{v\leftrightarrow l} = \begin{cases} h_{cond}\dfrac{\epsilon_p(1-s)x_v}{RT} & x_v p_g - p_{sat} > 0 \\ h_{evap}\dfrac{\epsilon_p s \rho_l}{M_{H_2O}} & x_v p_g - p_{sat} < 0 \end{cases} \tag{18}$$

h_{cond} and h_{evap} are the condensation and evaporation rate constants, whose values are taken from [25].

In a similar fashion, the vapour-dissolved phase-change term in Eqs. (2) and (6), $S_{v\leftrightarrow d}$, is driven by the deviation from equilibrium between the vapour and dissolved water, $c^d_{H_2O} - c^*_{H_2O}$, where $c^*_{H_2O}$ is the dissolved water concentration at equilibrium, as given in [33]:

$$\lambda^* = 0.3 + 10.8 a_w - 16 a_w^2 + 14.1 a_w^3, \tag{19}$$

or, equivalently:

$$c^*_{H_2O}(u_2 + 0.0126\lambda^*) = \lambda^*. \tag{20}$$

In these formulae, $a_w = x_v p_g / p_{sat}$ is the water vapour activity. The mass-transfer coefficient $h_{v\leftrightarrow d}$ is approximated from the results in [34]:

$$h_{v\leftrightarrow d} = \begin{cases} h_{ads,v}(1-s)\lambda & c^d_{H_2O} - c^*_{H_2O} < 0 \\ h_{des,v}(1-s)\lambda & c^d_{H_2O} - c^*_{H_2O} > 0, \end{cases} \tag{21}$$

where $h_{des,v}$ and $h_{ads,v}$ are desorption and adsorption coefficients, respectively. Their values are given in Table 10.

The equilibrium membrane water content depends on its environment, with either relationship (19) for contact with vapour or $\lambda = \lambda^l = 16.8$ for contact with liquid water. Note that the liquid-equilibrated dissolved water concentration, $c^l_{H_2O}$, is given by Eq. (7):

$$c^l_{H_2O} = \frac{\lambda^l}{u_2 + 0.0126\lambda^l}.$$

The discontinuity between the vapour-saturated and liquid values is known as Schroeder's paradox. The mass-transfer term $S_{d\leftrightarrow l}$ in Eqs. (6) and (8), and Table 2, is decomposed into terms for absorption and desorption of liquid water to and from the electrolyte in the catalyst layer. When the liquid-equilibrated water content value $c^l_{H_2O}$ is reached or exceeded, it is assumed that desorption of water from the electrolyte takes place (as liquid), the magnitude of which is driven by $c^d_{H_2O} - c^l_{H_2O}$. Adsorption is assumed to take place for $c^d_{H_2O} < c^l_{H_2O}$ provided $s > s_*$, where s_* is the immobile saturation. The coefficient $h_{d\leftrightarrow l}$ in Table 2 therefore takes the form:

$$h_{d\leftrightarrow l} = h_{des,l} H(c^d_{H_2O} - c^l_{H_2O}) + h_{ads,l} H(s - s_*) H(-c^d_{H_2O} + c^l_{H_2O}), \tag{22}$$

where $H(\cdot)$ is the Heaviside function and $h_{des,l}$ and $h_{ads,l}$ are the coefficients of desorption and absorption, which, for simplicity, are assumed to be constant. Their values are given in Table 10.

2.2. Reaction kinetics

The reaction rates appearing in Tables 2 and 3 are yet to be defined. The kinetics at the cathode are approximated by the following global, one-step reaction:

$$\text{Oxygen reduction reaction (ORR)}: \quad O_2 + 4H^+ + 4e^- \rightleftharpoons 2H_2O, \tag{23}$$

for which we use the Butler–Volmer law (in mol m^{-3} s^{-1}):

$$q_{O_2}(\eta_c, T, c^s_{O_2}) = \frac{a j_{O_2,ref}}{F c_{O_2,ref}} \epsilon_e c^s_{O_2} \left\{ \exp\left(\frac{\alpha_a F \eta_c}{RT}\right) - \exp\left(-\frac{\alpha_c F \eta_c}{RT}\right) \right\}. \tag{24}$$

The various terms in the formula are the exchange current density $j_{O_2,ref}$; the anodic and cathodic transfer coefficients α_a and α_c,

respectively; the reference oxygen molar concentration $c_{O_2,ref}$; the volumetric specific surface area of catalyst (per unit volume of catalyst layer) a; and the overpotential η_c. The expression

$$a = \frac{a_{pt} m_{pt}}{L}$$

relates the specific surface area of platinum to the mass specific platinum surface area (platinum surface area per unit mass of platinum), a_{pt}, the platinum loading, m_{pt}, and the catalyst layer thickness, L. The overpotentials in the cathode and anode, η_c and η_a respectively, are defined as

$$\eta_c = \phi_s - \phi_e - E_0, \quad \eta_a = \phi_s - \phi_e, \tag{25}$$

where E_0 is the open circuit potential *vs.* S.H.E. [35]:

$$E_0 = 1.23 - 9 \times 10^{-4}(T - 298.15).$$

An agglomerate model is used for the cathode catalyst layer, in which $c^s_{O_2}$ is the oxygen concentration at the agglomerate surfaces. It is related to the bulk value, c_{O_2}, by balancing the rate of reaction with the rate of diffusion of reactant through electrolyte and water films to the surfaces of the agglomerates. The final form of the reaction rate is

$$q_{O_2} = 4\gamma a' c_{O_2} \frac{e^{\alpha_a F\eta_c/RT} - e^{-\alpha_c F\eta_c/RT}}{\gamma + a'(e^{\alpha_a F\eta_c/RT} - e^{-\alpha_c F\eta_c/RT})}, \tag{26}$$

where the parameter a' is given by

$$a' = \frac{a j_{O_2,ref}}{4F c_{O_2,ref}}$$

γ is a measure of the diffusion rate through the films (γ/a is the piston velocity) and takes the form:

$$\gamma = \frac{\left(A' D_l/\delta_l\right)\left(A D^d_{O_2}/\delta_e\right)}{A' D_l/\delta_l + A D^d_{O_2}/\delta_e}, \tag{27}$$

in which $A' = 4\pi(R_{agg} + \delta_e)^2 N$. In these expressions: δ_e and δ_l are the electrolyte and liquid-water film thicknesses respectively; N is the number of agglomerates per unit volume; $A = 4\pi R^2_{agg} N$ is the specific surface area of agglomerates, assuming that the entire surface area of each agglomerate is covered; R_{agg} is the agglomerate radius; and D_l is the diffusion coefficient of O_2 through liquid water. The film thicknesses, δ_e and δ_l, are defined in Table 6 and take account of electrolyte swelling. The reader is referred to [23] for derivations.

The H_2S kinetics on platinum were investigated by Contractor and Lal [10,11], who suggested that there are two adsorbed forms of sulfur, one strongly and one weakly bonded. Mathieu and Primet [12], proposed the following form for the surface reactions:

$$H_2S + Pt \rightleftharpoons Pt\text{-}S + H_2. \tag{R1}$$

$$Pt\text{-}H + H_2S \rightleftharpoons Pt\text{-}S + \frac{3}{2}H_2. \tag{R2}$$

These reactions occur in competition with the adsorption and electro-oxidation of hydrogen [24]:

$$H_2 + 2Pt \rightleftharpoons 2Pt\text{-}H. \tag{R3}$$

$$Pt - H \rightleftharpoons H^+ + e^- + Pt. \tag{R4}$$

Mohtadi et al. [1], suggested that platinum sulfide (Pt-S) can also be formed electrochemically according to reaction (R5) below. The same reaction was proposed by and Najdeker and Bishop [14], who further suggested that platinum disulfide (Pt-S_2) could be formed according to reaction (R6):

$$H_2S + Pt \rightleftharpoons Pt\text{-}S + 2H^+ + 2e^-. \tag{R5}$$

$$H_2S + Pt\text{-}S \rightleftharpoons Pt - S_2 + 2H^+ + 2e^-. \tag{R6}$$

According to the cyclic-voltammetry measurements in [10,13], the main species to form is in fact Pt-S.

The adsorbed sulfur can be oxidised via reaction with water, as shown in reactions (R7) and (R8) below. This mechanism was proposed by Loučka [4], and confirmed by Mohtadi et al. [13] and Wang et al. [18], in which the authors report the presence of sulfate ions:

$$Pt\text{-}S + 3\,H_2O \rightleftharpoons SO_3 + 6H^+ + 6e^- + Pt. \tag{R7}$$

$$Pt\text{-}S + 4\,H_2O \rightleftharpoons SO_4^{2-} + 8H^+ + 6e^- + Pt. \tag{R8}$$

The mechanism considered by Shi et al. [16] is an application of the general contamination model developed in [36]. After approximation, it consists essentially of the forward parts of reactions (R1), (R3) and (R8), the competitive adsorption of H_2 on platinum and the following reaction:

$$Pt\text{-}H + H_2S \rightarrow Pt\text{-}S + H_2 + H^+ + e^-$$

This reaction, though not supported by experiment, appears to have been included for consistency with the model in [36].

The model developed below includes reactions (R1)-(R7). Reaction (R6) is neglected as per the results of [10,13] and reaction (R8) is neglected for simplicity. It is not expected that the overall behaviour of the system will be altered qualitatively by these assumptions. The model incorporates the two main mechanisms of adsorption and oxidation, for both hydrogen and sulfur.

Equations for the evolutions of the site coverages for atomic hydrogen and sulfur, θ_H and θ_S respectively, are then as follows:

$$\tau \frac{d\theta_H}{dt} = -q_2 + 2q_3 - q_4 \tag{28}$$

$$\tau \frac{d\theta_S}{dt} = q_1 + q_2 + q_5 - q_7 \tag{29}$$

where the rates are defined by

$$\begin{aligned}
q_1 &= r_{1f} c^d_{H_2S} \theta_{Pt} \exp\left(-\frac{\alpha_1 i \theta_S}{RT}\right) - r_{1b} c^d_{H_2} \theta_S \exp\left(\frac{(1-\alpha_1) i \theta_S}{RT}\right)^{3/2} \\
q_2 &= r_{2f} \theta_H c^d_{H_2S} - r_{2b} \theta_S \left(c^d_{H_2}\right) \\
q_3 &= r_{3f} c^d_{H_2} \theta^2_{Pt} - r_{3b} \theta^2_H \\
q_4 &= r_4 \theta_H \sinh\left(\frac{\alpha_4 F \eta_a}{RT}\right) \\
q_5 &= r_{5f} c^d_{H_2S} \theta_{Pt} \exp\left(\frac{2\alpha_5 F \eta_a}{RT}\right) - r_{5b} \theta_S c^2_{H^+} \\
&\quad \times \exp\left(-\frac{2(1-\alpha_5) F \eta_a}{RT}\right) \\
q_7 &= r_{7f} \left(c^d_{H_2O}\right)^3 \theta_S \exp\left(\frac{6\alpha_7 F \eta_a}{RT}\right) \\
&\quad - r_{7b} c^d_{SO_3} c^6_{H^+} \theta_{Pt} \exp\left(-\frac{6(1-\alpha_7) F \eta_a}{RT}\right).
\end{aligned} \tag{30}$$

The quantity τ is the molar area density of catalyst sites. The surface coverage of free platinum sites, θ_{Pt}, is given by

$$\theta_{Pt} = 1 - \theta_H - \theta_S \tag{31}$$

Eqs. (30) and (31) are derived on the assumption that coverage does not exceed a monolayer. The forms of the reaction rates are based on:

(1) a Frumkin isotherm for reaction (R1), sulfur adsorption and desorption, with rate q_1;

(2) Langmuir isotherms for reaction (R2) and reaction (R3), H_2 dissociative adsorption and desorption, with rates q_2 and q_3 respectively;
(3) Butler–Volmer kinetics for reaction (R4), electro-oxidation of hydrogen, with rate q_4;
(4) and Butler–Volmer type kinetics for the oxidation reactions (R5) and (R7), with rates q_5 and q_7, respectively.

In the Frumkin model [37], the apparent standard free energy of adsorption is assumed to vary linearly with θ_S, with slope equal to the interaction parameter i, [38]. Since their values are not known, all charge transfer coefficients, α_i, are assumed to be 1/2. This is a common modelling assumption. It was further assumed that the backward rates for reactions (R5) and (R7) are negligibly small. The values of r_{1f}, r_{1b} and r_{7f} were then fitted to achieve a qualitative match to experimental results in the literature. Similar fitting procedures have been performed in [3,6,7,16].

2.3. Initial and boundary conditions

At the interfaces between the membrane and catalyst layers, $y = y_2$ and $y = y_3$ shown in Fig. 1, the gas-phase and liquid-water fluxes are taken to be zero. Similarly, the fluxes of protons and dissolved species at the interfaces between the catalyst and gas diffusion layers, $y = y_1$ and $y = y_4$, are negligibly small:

$$y = y_1,\ y_4: \quad \begin{cases} \epsilon^{3/2} D_i^d \dfrac{\partial c_i^d}{\partial y} = 0 \\ \epsilon^{3/2} \sigma_e \dfrac{\partial \phi_e}{\partial y} = 0 \\ D^d_{H_2O} \dfrac{\partial c^d_{H_2O}}{\partial y} + \dfrac{5\lambda\sigma_e}{44F\nu} \dfrac{\partial \phi_e}{\partial y} = 0 \end{cases} \tag{32}$$

$$y = y_2, y_3: \quad \begin{cases} D_i \dfrac{\partial c_i}{\partial y} - v_g c_i = 0 \\ \dfrac{\partial s}{\partial y} = 0 \end{cases} \tag{33}$$

At the interfaces between the channels and gas diffusion layers, the gas mole fractions are prescribed or calculated from the other conditions:

$$x_i = \begin{cases} \bar{x}_{i,c} & y = y_0 \\ \bar{x}_{i,a} & y = y_5 \end{cases}, \quad i = H_2, O_2, H_2S, SO_3, N_2, H_2O. \tag{34}$$

Likewise, temperature, water activity and pressure are prescribed according to the channel values:

$$\begin{aligned} &T(y_0) = T_c \quad T(y_5) = T_a, \\ &p_g(y_0) = p_c \quad p_g(y_5) = p_a, \\ &a_w(y_0) = a_{w,c} \quad a_w(y_5) = a_{w,a}. \end{aligned} \tag{35}$$

The concentrations of water vapour in the cathode and anode channels, $\bar{c}_{v,c}$ and $\bar{c}_{v,a}$ respectively, are calculated from the water activities and saturation pressures ([32]):

$$\begin{aligned} \log_{10} p_{sat} = -2.1794 &+0.02953(T - 273.15) \\ &-9.1837 \times 10^{-5}(T - 273.15)^2 \\ &+1.4454 \times 10^{-7}(T - 273.15)^3, \end{aligned} \tag{36}$$

in bars, yielding:

$$\bar{c}_{v,c} = \frac{a_{w,c} p_{sat,c}}{RT_c} \quad \text{or} \quad \bar{x}_{v,c} = \frac{a_{w,c} p_{sat,c}}{p_c}$$

where $p_{sat,c}$ is the cathode-channel saturation pressure (expressed in Pa). A similar calculation applies on the anode side where the channel saturation pressure is $p_{sat,a}$.

Table 4
Operating conditions assumed in the calculations, unless otherwise specified

Symbol	Quantity	Size
T_c	Cathode channel temperature	60 °C
T_a	Anode channel temperature	60 °C
$a_{w,c}$	Cathode channel water activity	0.9
$a_{w,a}$	Anode channel water activity	0.9
$\bar{x}_{O_2,c}$	Oxygen mole fraction in cathode channel[a]	0.21
$\bar{x}_{H_2,a}$	Hydrogen mole fraction in anode channel[a]	0.4
$\bar{x}_{SO_3,a}$	SO_3 mole fraction in anode channel[a]	0
$\bar{x}_{N_2,c}$	Nitrogen mole fraction in cathode channel[a]	0.79
$\bar{x}_{N_2,a}$	Nitrogen mole fraction in anode channel[a]	0.6
$\bar{c}_{H_2S,a}$	H_2S mole fraction in anode channel[a]	2 ppm
p_c	Gas pressure in the cathode channel	300 kPa
p_a	Gas pressure in the anode channel	300 kPa
$\bar{c}_{H_2O,c}$	Vapour concentration in cathode channel	6.38 mol m^{-3}
$\bar{c}_{H_2O,a}$	Vapour concentration in the anode channel	6.38 mol m^{-3}
β_j	Liquid-water removal constants (anode and cathode)[a]	0.075 m^{-1}
j_a	Applied current density	0.5 A cm^{-2}
E	Cell voltage	0.5 V

[a] After subtracting the vapour concentration.

For operation in the potentiostatic mode the cell voltage, E, is prescribed at the cathode channel/gas diffusion layer interface, and at the anode channel/gas diffusion layer interface the electronic potential is assigned a value of zero:

$$\phi_s(y_0) = E, \quad \phi_s(y_5) = 0. \tag{37}$$

When the cell is operated in galvanostatic mode, a current density j_a is prescribed at the electrode/gas channel interfaces:

$$-\sigma_p \frac{\partial \phi_s}{\partial y} = \begin{cases} j_a & y = 0 \\ -j_a & y = y_5 \end{cases} \tag{38}$$

where σ_p is the electronic conductivity of the current collector (plate).

The final boundary conditions are those for liquid water at the interfaces between the gas channels and the gas diffusion layer.

Table 5
The default parameter values relating to structural properties

Symbol	Quantity	Size
L	Catalyst layer thickness	25 μm
L_m	Membrane thickness	50 μm
L_G	GDL thickness	200 μm
ϵ_e^i	Electrolyte volume fraction in agglomerates[a]	0.15
ϵ_a	Volume fraction of agglomerates [40]	0.4215
ϵ_s	Volume fraction of carbon in CL[b]	0.2
ϵ_G	Porosity of the GDL [41]	0.74
R_{agg}	Agglomerate radius [40]	0.5 μm
$\delta_{e,0}$	Electrolyte film thickness without swelling [23]	0.1 μm
$\epsilon^f_{e,0}$	Electrolyte volume fraction without swelling [23]	$\frac{4\pi N}{3}[(R_{agg} + \delta_{e,0})^3 - R_{agg}^3]$
δ_e	Electrolyte film thickness [m] [23]	$\sqrt[3]{R_{agg}^3 + \frac{3\epsilon^f_e}{4\pi N}} - R_{agg}$
δ_l	Water film thickness [m]: $R_\delta = R_{agg} + \delta_e$[23]	$\sqrt[3]{R_\delta^3 + \frac{3s\epsilon_p}{4\pi N}} - R_\delta$
N	Agglomerate density[b]	5.8×10^{17} m^{-3}
a_{pt}	Specific surface area of platinum [42]	1000 cm^2(mg Pt)$^{-1}$
m_{pt}	Platinum loading[a]	0.4 (mg Pt) cm^{-2}
χ_C	Catalyst-layer contact angle [43]	90°
χ_G	Gas diffusion layer contact angle [43]	120°
d_G	GDL pore size[a]	10 μm
d_C	Catalyst-layer pore size[a]	2 μm

[a] Assumed value.
[b] Estimated value.

They are approximated using the following steady-state flux conditions at $y = y_0$ and $y = y_5$ (see [23] for details):

$$\frac{\partial s}{\partial y} - \beta_j s = 0, \quad j = \text{a,c}, \tag{39}$$

where $\beta_j = 0$ corresponds to zero water removal from the anode channel, j = a, or cathode channel, j = c.

The initial conditions for the pressures, temperatures and vapour concentrations are consistent with the conditions in the channels. The electronic potential at the initial time is given by the open-circuit potential at the cathode and is zero at the anode. The initial protonic potential is zero in all regions. The cell voltage or current is ramped at a finite rate as discussed later. The initial water content of the membrane/electrolyte is given by equilibrium with the vapour in the channels. The initial liquid-water saturation and all surface coverages are uniformly equal to zero at the initial time.

2.4. Numerical details and parameters

The initial-boundary value problem developed above was solved in the software package COMSOL Multiphysics® on a uniform grid (typically 128 points) using quartic Lagrange polynomials as trial and test functions. The relative tolerance was set to a value of 1×10^{-6} and the absolute tolerance to 1×10^{-8}. The switch functions were substituted with hyperbolic tangent functions to smooth the discontinuities.

The default set of parameter values is given in Tables 4–10 . Several parameters are estimated, as indicated in Tables 4–10, and the rest are found from the literature with references provided. Where available, values for Nafion were used. For several mass transport and transfer parameters, values corresponding to liquid water have been used as estimates. The pore size and porosity values fall within typical ranges for conventional PEMFC [39] and variations would not qualitative affect the results in this work.

The kinetic parameters were taken from the literature where available. In the absence of primary experimental data, the

Table 6
The default parameter values relating to electrochemical properties

Symbol	Quantity	Size
$j_{O_2,ref}$	Cathode exchange current density [22]	10^{-2} A m^{-2}
$c_{O_2,ref}$	Reference O_2 concentration[a]	0.05 mol m^{-3}
α_c	Cathodic charge transfer coefficient	0.55
α_a	Anodic charge transfer coefficient	0.45
α_1	Charge transfer coefficient for reaction (R1)[a]	0.5
α_4	Charge transfer coefficient for reaction (R4)[a]	0.5
α_5	Charge transfer coefficient for reaction (R5)[a]	0.5
α_7	Charge transfer coefficient for reaction (R7)[a]	0.5
i	Interaction parameter[a]	10 kJ mol^{-1}
τ	Molar area density of platinum sites [7]	0.01042 mol m^{-2}
r_{1f}	Forward rate constant: reaction (R1)[b]	3×10^{-2} m s^{-1}
r_{1b}/r_{1f}	Backward rate constant: reaction (R1)[a]	1.4×10^{-6}
r_{2f}	Forward rate constant: reaction (R2)[b]	1×10^{-2} m s^{-1}
r_{2b}/r_{2f}	Backward rate constant: reaction (R2)[a]	1×10^{-6} m$^{3/2}$ mol$^{-1/2}$
r_{3f}	Forward rate constant: reaction (R3) [44]	$3e^{-10400/RT}$ m s^{-1}
r_{3b}/r_{3f}	Backward rate constant: reaction (R3) [44]	4.18×10^{11} $e^{-87900/RT}$ mol m^{-3}
r_{4f}	Forward rate constant: reaction (R4) [44]	$23.1e^{-16700/RT}$ mol m^{-2} s^{-1}
r_{5f}	Forward rate constant: reaction (R5)[a]	1×10^{-4} m s^{-1}
r_{7f}	Forward rate constant: reaction (R7)[b]	4×10^{-12} m^7 s^{-1} mol^{-2}

[a] Assumed value.
[b] Fitted value.

Table 7
Parameters for the gas-phase diffusion coefficient in Eq. (3)

Symbol	Quantity	Size
σ_{O_2}	O_2 collision diameter [29]	3.433 Å
σ_{H_2}	H_2 collision diameter [29]	2.915 Å
σ_{vapour}	Vapour collision diameter [29]	2.903 Å
σ_{N_2}	N_2 collision diameter [29]	3.667 Å
σ_{H_2S}	H_2S collision diameter [29]	3.748 Å
σ_{SO_3}	SO_3 collision diameter [29]	4.29 Å
Ω_{N_2,O_2}	O_2–N_2 collision integral [29]	0.966
Ω_{N_2,H_2}	H_2–N_2 collision integral [29]	0.848
$\Omega_{N_2,vapour}$	Vapour–N_2 collision integral [29]	1.305
Ω_{N_2,N_2}	N_2–N_2 collision integral [29]	0.949
Ω_{H_2,N_2S}	H_2S–N_2 collision integral [29]	1.129
Ω_{N_2,SO_3}	SO_3–N_2 collision integral [29]	1.06
M_{O_2}	Molar mass of O_2	0.0032 kg mol^{-1}
M_{H_2}	Molar mass of H_2	0.0002 kg mol^{-1}
M_{H_2O}	Molar mass of H_2O	0.0018 kg mol^{-1}
M_{N_2}	Molar mass of N_2	0.0028 kg mol^{-1}
M_{H_2S}	Molar mass of H_2S	0.0034 kg mol^{-1}
M_{SO_3}	Molar mass of SO_3	0.008 kg mol^{-1}

Table 8
Default parameter values related to mass transport

Symbol	Quantity	Size
$D^d_{O_2}$	O_2 diffusion coefficient in the electrolyte[a],[45]	$3.1 \times 10^{-7}e^{-2768/T}$ m^2 s^{-1}
$D^d_{H_2}$	H_2 diffusion coefficient in the electrolyte[a],[46]	6.92×10^{-9} m^2 s^{-1}
$D^d_{H_2S}$	H_2S diffusion coefficient in the electrolyte[a]	4.38×10^{-9} m^2 s^{-1}
$h_{pe,i}$	Mass transfer rates[b]	10^5 s^{-1}
κ_C	Absolute permeability of CCL [47]	10^{-13} m^2
κ_G	Absolute permeability of GDL [47]	8.7×10^{-12} m^2
μ_l	Liquid water viscosity	10^{-3} Pa s
μ	Dynamic viscosity: air[b]	1.8×10^{-5} Pa s
μ	Dynamic viscosity: H_2[b]	8.4×10^{-6} Pa s
σ'	Surface tension [26]	0.07 N m^{-1}
σ_s	Electronic conductivity	500 S m^{-1}

[a] Approximated by value in/for liquid water at 60 °C.
[b] Estimated.

Table 9
Default parameter values related to mass transfer

Symbol	Quantity	Size
H_{O_2}	O_2 Henry's law constant [48]	0.15
H_{H_2}	H_2 Henry's law constant [49]	0.63
H_{H_2S}	H_2S Henry's law constant	0.32
H_{SO_3}	SO_3 Henry's law constant	1.94
$h_{des,l}$	Desorption coefficient of dissolved to liquid water[a]	100
$h_{ads,l}$	Adsorption coefficient of liquid to dissolved water[a]	10
$h_{ads,v}$	Absorption coefficient of vapour to dissolved water [34]	1×10^{-6} m s^{-1}
$h_{des,v}$	Desorption coefficient of dissolved water to vapour [34]	3.3×10^{-6} m s^{-1}
h_{evap}	Evaporation coefficient [25]	100 s^{-1} atm^{-1}
h_{cond}	Condensation coefficient [25]	100 s^{-1}
λ^*_l	Liquid-equilibrated water content [25]	16.8

[a] Assumed value.

Table 10
Default parameter values for the heat equation

Symbol	Quantity	Size
k	Catalyst layer thermal conductivity [50]	0.67 W m^{-1} K^{-1}
k_m	Membrane thermal conductivity [50]	0.67 W m^{-1} K^{-1}
k_G	GDL thermal conductivity [50]	1.67 W m^{-1} K^{-1}
$\rho_l C_l$	H_2O thermal capacitance	4.187×10^6 J m^{-3} K^{-1}
$\rho_g C_g$	Gas phase thermal capacitance/air	10^3 J m^{-3} K^{-1}
$\rho_m C_m$	Membrane thermal capacitance[a]	2.18×10^6 J m^{-3} K^{-1}
$\rho_{carb} C_{carb}$	Carbon phase thermal capacitance	1.61×10^6 J m^{-3} K^{-1}
$-\Delta s_c$	Entropy associated with ORR [51]	163.7 J mol^{-1} K^{-1}
$-\Delta s_a$	Entropy associated with HOR [51]	0 J mol^{-1} K^{-1}

[a] Estimated.

values for r_{1b}/r_{1f}, r_{2b}/r_{2f} and r_{5f} were assigned arbitrarily and the values for r_{1f}, r_{2f} and r_{7f} were fitted to the provided a qualitative match to the values and trends in [1,16]. As confirmation of the values, the fitted adsorption rate constant r_{1f} was compared to that approximated from experimental data at different temperatures by Mohtadi et al. in [1]. Their predicted value is of the same order of magnitude, $O(10^{-2})$, as that shown in Table 6.

In the next section use will be made of the spatially averaged reaction rates and surface coverages. These are defined as the integrals of the reaction rates or surface coverages in space over the anode catalyst layer, normalised with respect to L, the length of the catalyst layer:

$$\langle q_i \rangle = \frac{1}{L}\int_{ACL} q_i \, dy$$
$$\langle \theta_S \rangle = \frac{1}{L}\int_{ACL} \theta_S \, dy \tag{40}$$
$$\langle \theta_H \rangle = \frac{1}{L}\int_{ACL} \theta_H \, dy.$$

The **terminal** value of a quantity $\psi(t)$ will be defined as the value of ψ at steady state, i.e.:

$$\text{“Terminal value of } \psi(t)\text{”} = \psi(\infty). \tag{41}$$

3. Results and discussion

3.1. Basic features and validation

Fig. 2 shows simulation results at different current densities, at a fixed H_2S concentration of 2 ppm, and different H_2S concentrations, at a fixed current density of 0.5 A cm^{-2}. The simulations are of

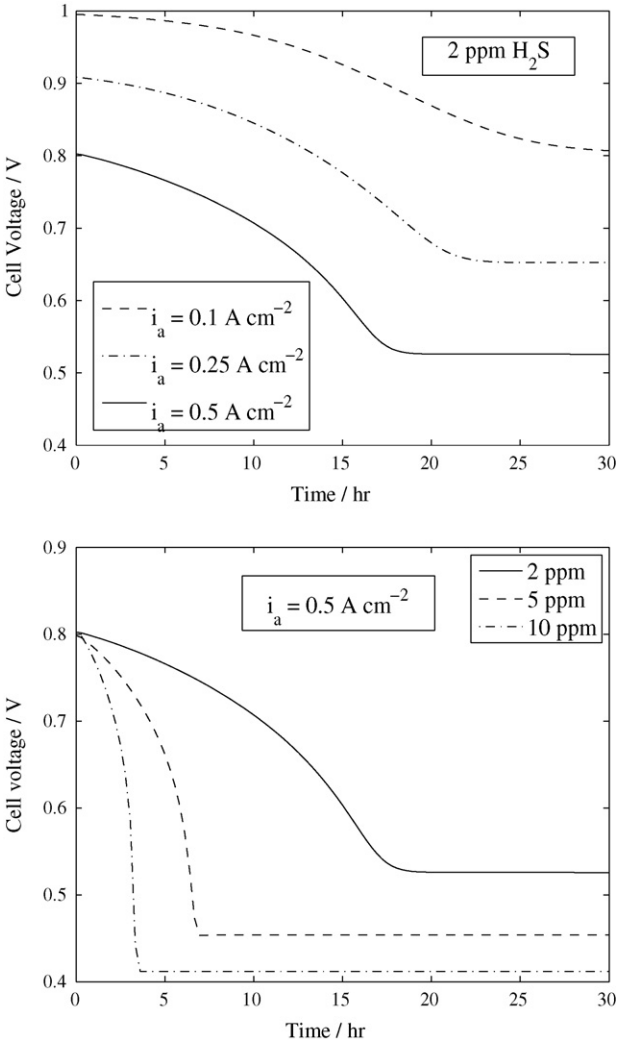

Fig. 2. The effect of H_2S concentration and current density on the extent of poisoning when operating in galvanostatic mode. See Tables 4–10 for values of the other parameters.

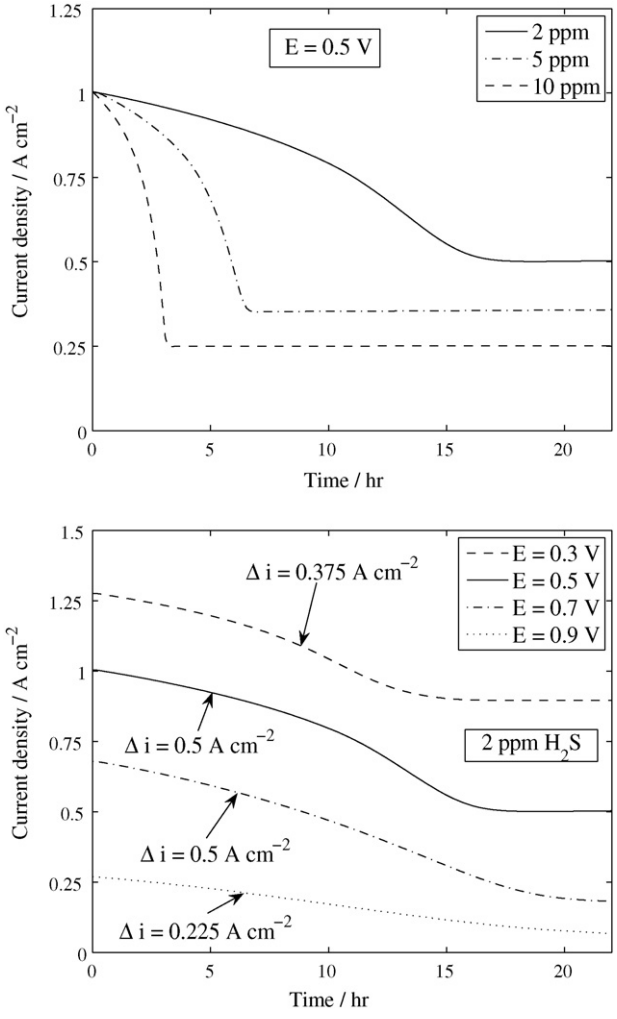

Fig. 3. The effect of H_2S concentration (top figure) and cell voltage (bottom) on the extent of performance loss when operating in potentiostatic mode. In the top figure the cell voltage is fixed at 0.5 V and in the bottom figure the H_2S concentration is fixed at 2 ppm. The temperature is 60° C in both figures. See Tables 4–10 for values of the other parameters.

operation in the galvanostatic mode. The hydrogen source in these simulations is 40% H_2 in N_2. The other parameter values are given in Tables 4–10 and are used throughout, unless otherwise stated. These tables also contain the default values of current density, voltage and H_2S concentration. In each simulation the initial conditions were generated from a gradual increase in the current over a period of 500 s from 0 A cm^{-2}, and 0 ppm H_2S, to the stated current density value, followed by 2 h at this current density. A steady state was reached in each case.

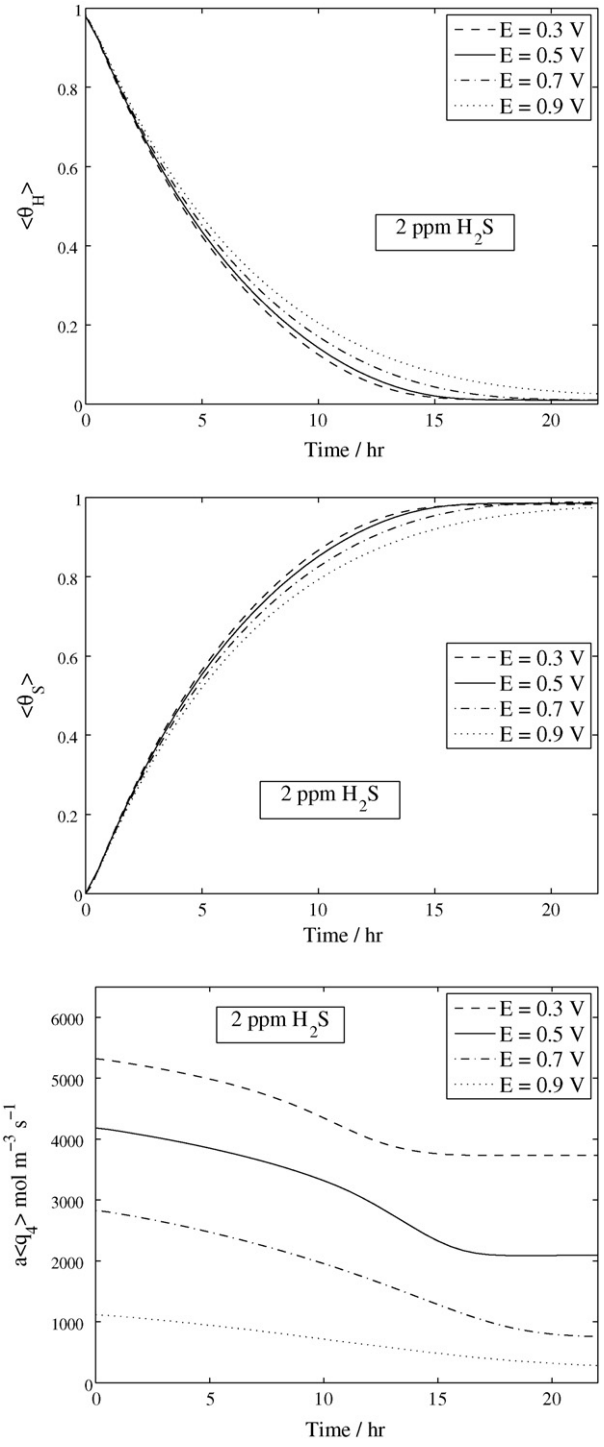

Fig. 4. The evolutions of the average values of the hydrogen oxidation rate, q_4, and the surface coverages of sulfur and hydrogen, $a\langle q_4\rangle$, $\langle\theta_S\rangle$ and $\langle\theta_H\rangle$, respectively, at different cell voltage values with an H_2S concentration of 2 ppm and at a temperature of 60 °C. See Tables 4–10 for values of the other parameter. Table 11 shows the terminal values of $\langle\theta_S\rangle$ and $\langle\theta_H\rangle$.

Table 11
Terminal values of the spatially averaged surface coverages of hydrogen and sulfur, $\langle\theta_H\rangle$ and $\langle\theta_S\rangle$respectively, corresponding to the calculations in Figs. 3 and 4

Cell voltage (V)	Terminal $\langle\theta_S\rangle$	Terminal $\langle\theta_H\rangle$
0.3	0.9826	0.01085
0.5	0.9862	0.00987
0.7	0.9895	0.00975
0.9	0.9830	0.01082

The H_2S concentration is 2 ppm and the channel temperatures are 60 °C. See Tables 4–10 for values of the other parameters.

In both cases, the results in Fig. 2 results capture precisely the trends observed in the experiments of Shi et al. [16]. As the current density is increased at fixed H_2S concentration the extent of poisoning (decrease in cell voltage) increases. As the H_2S concentration is increased at a fixed current density the degree of poisoning again increases.

Fig. 3 shows simulation results in the potentiostatic mode at different values of H_2S concentration and cell voltage, again with 40% H_2 in N_2. In these simulations the initial conditions were generated from a gradual increase in the cell voltage over a period of 500 s from the open circuit potential, and 0 ppm H_2S, to the stated

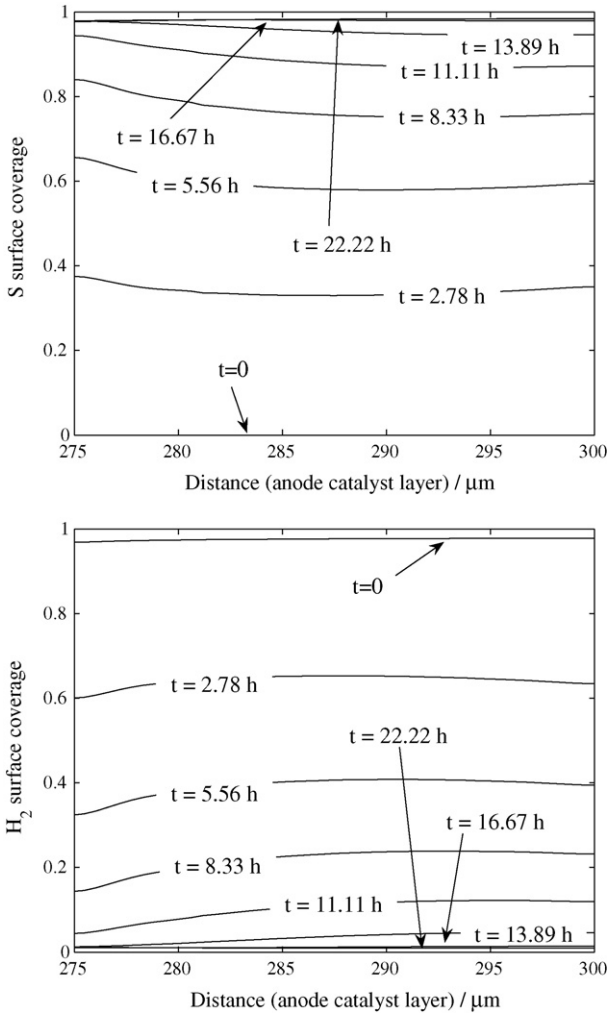

Fig. 5. The evolutions of the profiles of sulfur and hydrogen surface coverages during poisoning, corresponding to the calculation at a cell voltage of 0.5 V with 2 ppm H_2S in Fig. 3. See Tables 4–10 for values of the other parameters.

cell voltage value, followed by operation at this cell voltage until a steady state was reached.

As the H_2S concentration is increased at a fixed cell voltage of 0.5 V, the drop in current density as a result of poisoning increases. The profiles are a good fit to the transient data in [1,18] showing the decay of the anode current density. The trend with respect to variations in cell voltage at a fixed H_2S concentration indicates that the degree of poisoning initially increases as the cell voltage is decreased, but as the cell voltage is lowered further, performance improves; that is seen by comparing the current density changes from the initial time to steady state, Δi, shown in Fig. 3. This result is caused by the trend in the rate of hydrogen oxidation from the platinum surfaces, reaction (R4), as the cell voltage is lowered. Fig. 4 shows the evolutions of the spatially averaged hydrogen oxidation rate, $a\langle q_4\rangle$, the spatially averaged surface coverage of sulfur, $\langle\theta_S\rangle$, and the spatially averaged surface coverage of hydrogen, $\langle\theta_H\rangle$. In these figures the cell voltage is varied from 0.9 to 0.3 V with 2 ppm H_2S at an operating temperature of 60 °C, as in Fig. 3.

The variation in current density in Fig. 3 as the cell voltage is lowered mirrors the variation in $a\langle q_4\rangle$, clearly demonstrating that the oxidation of hydrogen controls the extent of degradation. The terminal values of $\langle\theta_S\rangle$ and $\langle\theta_H\rangle$, defined in Eq. (41), are shown in Table 11. The terminal value of $\langle\theta_H\rangle$ decreases as the cell voltage is increased from 0.3 to 0.5 V and again from 0.5 to 0.7 V. On the other hand, the terminal value of $\langle\theta_H\rangle$ *increases* as the cell voltage is increased from 0.7 to 0.9 V. Correspondingly, the terminal value of $\langle\theta_S\rangle$ increases from 0.3 to 0.7 V and decreases from 0.7 to 0.9 V. This would suggest that as the cell voltage is lowered the extent of degradation, measured by the drop in current density, reaches a maximum, which is indeed the case in Fig. 3.

Fig. 5 shows the evolution of the surface coverage profiles during the calculation at 0.5 V with 2 ppm H_2S. At the initial time, when the concentration of H_2S is increased from 0 to 2 ppm, the coverage of platinum sites by hydrogen is almost complete. Within 2.78 h roughly 40% of the surface area is covered by sulfur, with a corresponding decrease in adsorbed hydrogen. Thereafter, the adsorption rate of sulfur is increasingly slower but at the terminal current density the surface coverage of sulfur is close to a monolayer: $\theta_S \approx 1$.

3.2. Effect of channel temperature and water activity

The effect of temperature on the extent of poisoning is depicted in Fig. 6, showing simulation results at different channel temperatures for an H_2S concentration of 2 ppm and a cell voltage of 0.5 V. It is immediately noticeable that the initial current density increases as the channel temperature is increased. There are several effects associated with a temperature increase at fixed values of other quantities in the absence of H_2S: a decrease in the channel concentration of reactants; a decrease in the reaction rates for oxygen reduction and hydrogen oxidation through the Arrhenius dependence; a decrease in the rate of condensation through an increase in the saturation vapour pressure and a reduction in the channel vapour concentration; and an increase in the membrane conductivity. The latter effect dominates, leading to the higher initial current density.

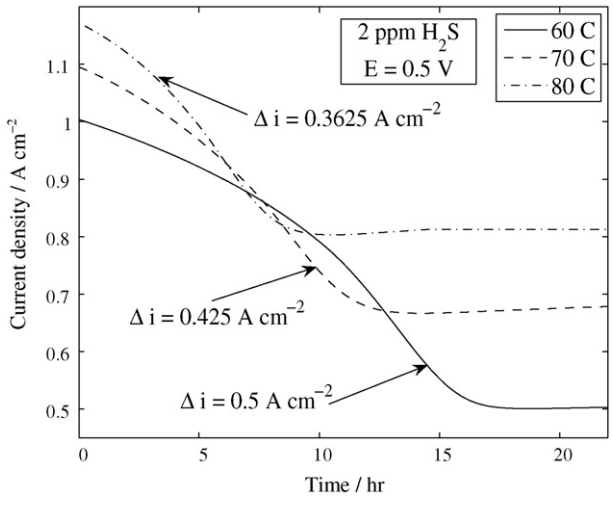

Fig. 6. The effect of channel temperature on H_2S poisoning: for an H_2S concentration of 2 ppm and a cell voltage of 0.5 V. See Tables 4–10 for values of the other parameters.

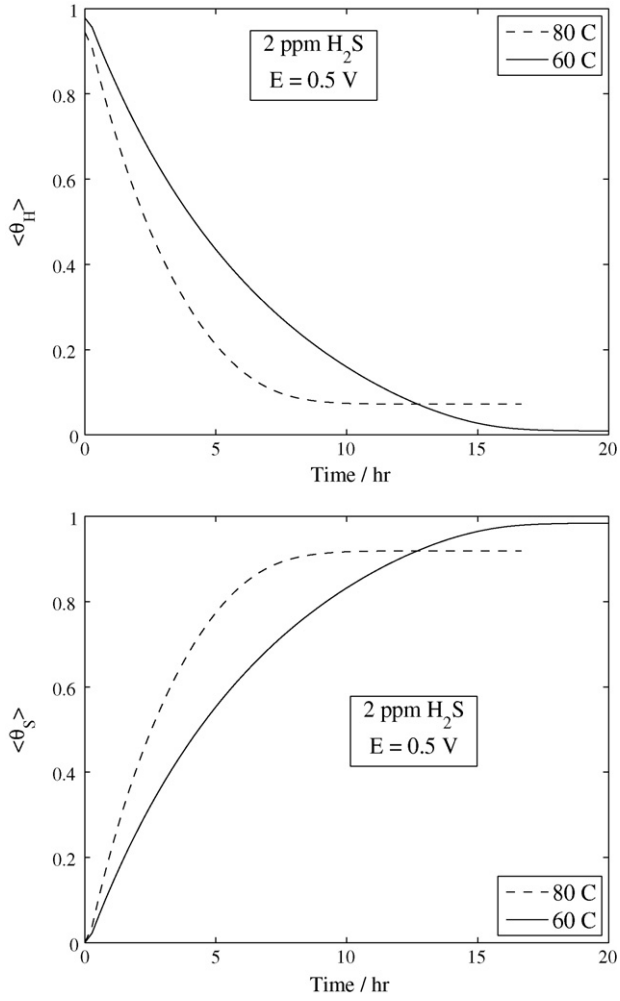

Fig. 7. The evolution of the spatially averaged surface coverages of sulfur and hydrogen, $\langle\theta_S\rangle$ and $\langle\theta_H\rangle$, respectively, corresponding to the calculations at channel temperatures of 60 and 80 ° C shown in Fig. 6. See Tables 4–10 for values of the other parameters.

As the channel temperature is increased the drop in current density from its initial to terminal value decreases, leading to a reduced degree of poisoning. This can bee seen from the current density changes, Δi, shown in Fig. 6 at each temperature. Fig. 7 shows the evolution of the spatially averaged surface coverages of sulfur and hydrogen defined in Eq. (40), corresponding to the calculations at 60 and 80 ° C in Fig. 6. These plots demonstrate that the reduced degree of poisoning is the result of a greater terminal coverage of hydrogen and a lower terminal coverage of sulfur at the higher temperature.

However, Fig. 7 also shows that the coverage of platinum sites by sulfur is more rapid as the temperature is increased, so that θ_S is higher and θ_H is lower up to approximately $t = 13$ h, at which point the curves intersect. Thus, although poisoning is less severe at the higher temperature on a long time scale, the rate of poisoning is faster, i.e., the current density drops more rapidly. Indeed the two curves at 60 and 80 ° C in Fig. 6 intersect at approximately $t = 7$ h.

The above result agrees with the experimental data of Mohtadi et al. [1], in which the authors estimate the surface coverage of sulfur at different temperatures by dividing the oxidation charge by the maximum total charge obtained under sulfur saturation conditions. More precisely, the shape of the profiles of $\langle\theta_S\rangle$ and the trend with respect to temperature in Fig. 7, before a steady state is established, match the shape and trend in Fig. 4 of [1]. The timescales are also very similar. Mohtadi et al. do however estimate that the surface coverage of sulfur at long times increases with temperature, which seems not to support the crossing of the curves in Fig. 7. The authors also state that the half-cell current decrease at 90 ° C was lower than the current decrease corresponding to the same sulfur coverage for full cells at 70 and 50 °C. Therefore they chose not to base the coverage calculations on the current decrease. They hypothesise that sulfur crosses over to the cathode, thus affecting the oxygen reduction reaction. Furthermore, the full-cell curves at 50 and 70 ° C in Fig. 7 of their paper were found to cross at intermediate times before a steady state was established, in a manner similar to that in Fig. 6. The results are therefore inconclusive. Certain elements of the results displayed in Figs. 6 and 7 can be validated, but the behaviour seen as the steady states are approached cannot be confirmed until further data is available. On the other hand several of the results in [1] seem to support it. The following hypothesis, to be discussed below, is made: *the nonlinear behaviour found in [1] is due to the competition between adsorption and oxidation of sulfur*.

To investigate the behaviour described above the reader is referred to Fig. 8, which shows the corresponding evolutions at both temperatures of the spatially averaged rates of the surface reactions (R1), (R3), (R4) and (R7), defined in Eq. (40): $a\langle q_1\rangle$, $a\langle q_3\rangle$, $a\langle q_4\rangle$ and $a\langle q_7\rangle$. These are sulfur adsorption, hydrogen adsorption, hydrogen oxidation and sulfur oxidation respectively. In both cases the average rate of sulfur adsorption, $a\langle q_1\rangle$, rises rapidly as the fuel source is changed from clean to contaminated. The terminal value of $a\langle q_1\rangle$ increases as the temperature is increased, and $a\langle q_1\rangle$ relaxes to a steady-state value in a shorter period of time. At fixed θ_S and θ_{Pt}, the forward part of the reaction rate q_1 in Eq. (29) increases and the backward part decreases as temperature is increased. The result is a higher value of θ_S at 80 ° C during the early stages of its evolution (before steady state). This occurs in competition with the increased adsorption rate of hydrogen shown in Fig. 8. As θ_S increases the sulfur adsorption rate decreases (a consequence of the Frumkin kinetics), and thus a steady state is reached sooner. On the other hand, the average oxidation rate of sulfur, $a\langle q_7\rangle$, is greater at the higher temperature. The relative increase in the terminal value of $a\langle q_7\rangle$, that is

$$\frac{\text{terminal value at } 80\,^\circ\text{C} - \text{terminal value at } 60\,^\circ\text{C}}{\text{terminal value at } 60\,^\circ\text{C}}$$

is equal to 1.9167, while the relative increase in the terminal value of $a\langle q_1\rangle$ is 1.727, which further suggests that the terminal value of θ_S should be lower at 80 °C. This is indeed the case in Fig. 7. In other words, the increase in the adsorption rate of sulfur at 80 ° C is dominated by the simultaneous increase in its oxidation rate. The equivalent relative increases in $a\langle q_3\rangle$ and $a\langle q_4\rangle$ are almost identical (approximately 0.62) implying that the increased adsorption

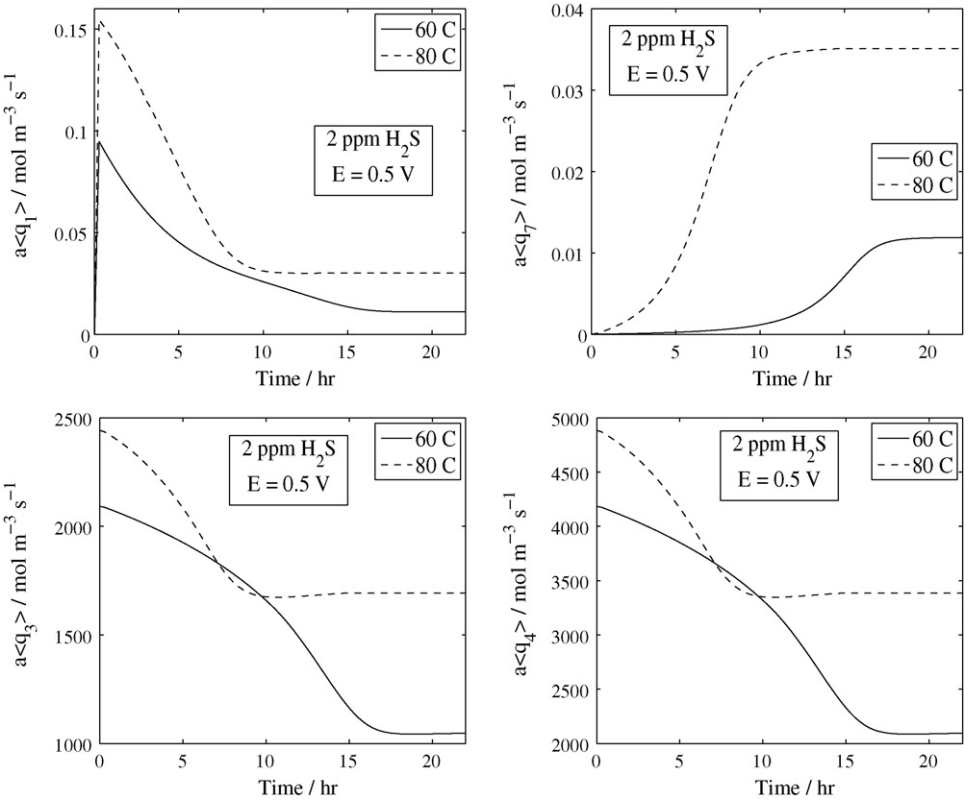

Fig. 8. The evolution of the spatially averaged rates of the surface reactions (R1), (R3), (R4) and (R7), $a\langle q_1\rangle$, $a\langle q_3\rangle$, $a\langle q_4\rangle$ and $a\langle q_7\rangle$, respectively, for the two cases 60 and 80 ° C shown in Fig. 6. See Tables 4–10 for values of the other parameters.

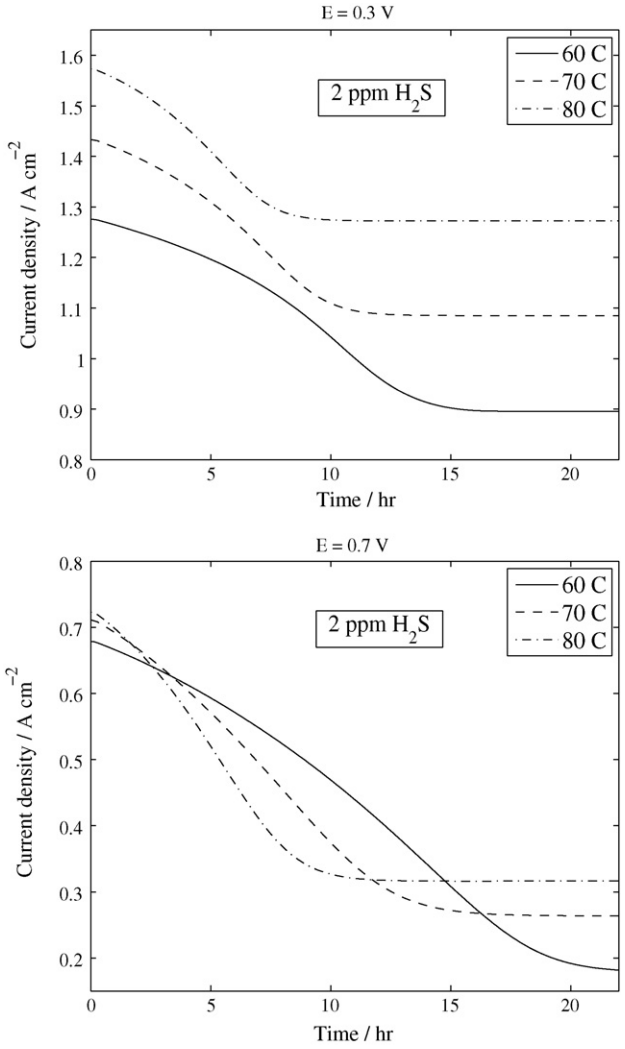

Fig. 9. The effect of simultaneous changes in the channel temperature and cell voltage on H_2S poisoning: for an H_2S concentration of 2 ppm. See Tables 4–10 for values of the other parameters.

of atomic hydrogen is dominated by its increased oxidation. The higher terminal value of θ_H at 80° C is therefore a direct consequence of the lower terminal value of θ_S. Note finally that the reaction rates for sulfur are much smaller than those for hydrogen, which is due to the very small H_2S concentrations.

These results pertain to a cell voltage of 0.5 V. To see the effect of changes in the cell voltage as the channel temperature is varied, the reader is referred to Fig. 9. As the cell voltage is increased, the difference in the terminal current density between 60 and 80° C decreases. For example, at $E = 0.3$ V the difference is approximately 0.37 A cm^{-2} and at $E = 0.7$ V it is approximately 0.14 A cm^{-2}. Moreover, there is a qualitative difference between the two sets of curves in Fig. 9; at $E = 0.3$ V performance is uniformly better at higher temperature, whereas at $E = 0.7$ the performance at lower temperature is superior except towards the beginning of the calculation and towards the end after the terminal current density has been reached at the higher temperature; performance at 60° C is better than performance at 70° C between $3.39 < t < 16.26$ h. For both $E = 0.3$ V and $E = 0.7$ V, Fig. 10 shows the evolutions of $a\langle q_1\rangle$ and $a\langle q_7\rangle$ at 80° C and Fig. 11 shows the evolutions of $a\langle q_1\rangle$ and $a\langle q_7\rangle$ at 60 °C. At 60 °C, there is a visible delay in the times taken for both $a\langle q_1\rangle$ and $a\langle q_7\rangle$ to relax to their steady-state values. In contrast, the differences in these times at 80° C are slight. Thus, while at 80° C the rate of poisoning changes little when the cell voltage is decreased from 0.7 to 0.3 V, at 60° C it visibly increases. This, allied with the increasing differences in initial current densities as the cell voltage is increased, explains why the curves in Fig. 9 intersect at 0.7 V but not at 0.3 V.

One of the main performance control mechanisms in PEM fuel cells is the channel water activity, which must be chosen such that the membrane remains well hydrated for sufficiently high protonic conductivity and such that flooding does not occur in the cathode catalyst layer, restricting reactant access to the catalyst sites. Fig. 12 shows the effect of variations in the water activity (the same in both channels) at a cell voltage of 0.5 V and with 2 ppm H_2S in 40% H_2/N_2. All other parameters are fixed as in Tables 4–10. The plots reveal an improvement in performance in going from $a_w = 0.7$ (equilibrium relative humidity of 70%) to $a_w = 1$ in both channels. However, for water activities below 0.7, very little change in the performance is seen.

It is instructive to examine the water saturation profiles for the two cases of $a_w = 1$ and $a_w = 0.7$; these are shown in Fig. 13. Immediately noticeable is that the saturation levels in the case $a_w = 0.7$ are lower, clearly as a result of the reduced rates of condensation. The levels in the anode are practically zero and are not therefore visible in these plots. The second feature to notice is that the saturation levels fall markedly during the poisoning process. In the cathode the lower current density due to poisoning reduces the

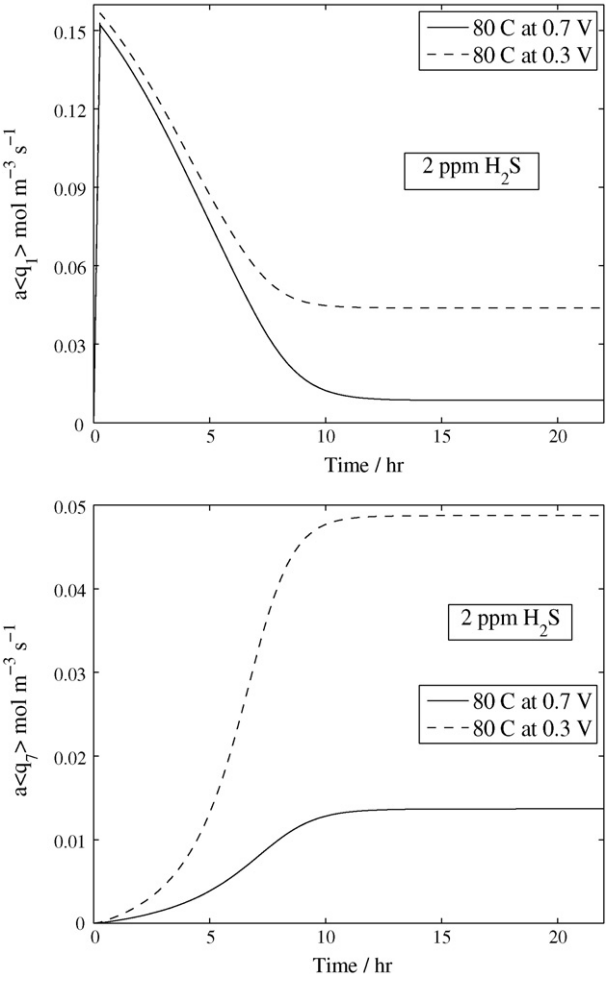

Fig. 10. The evolutions of the spatially averaged rates of the surface reactions (R1) and (R7), $a\langle q_1\rangle$ and $a\langle q_7\rangle$, respectively, for the case 80° C shown in Fig. 9. See Tables 4–10 for values of the other parameters.

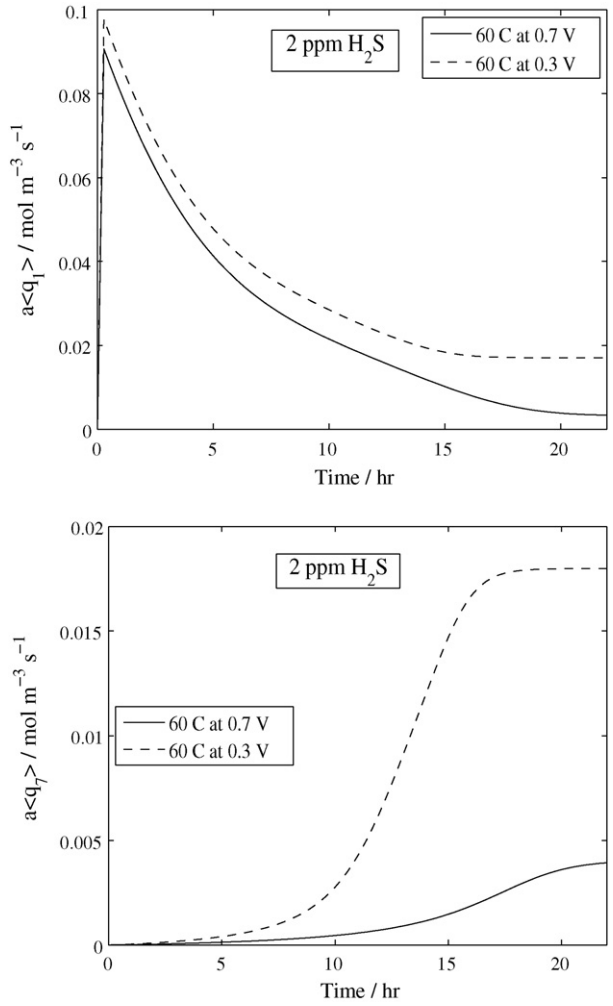

Fig. 11. The evolutions of the spatially averaged rates of the surface reactions (R1) and (R7), $a\langle q_1\rangle$ and $a\langle q_7\rangle$, respectively, for the case 60° C and 2 ppm H_2S. See Tables 4–10 for values of the other parameters.

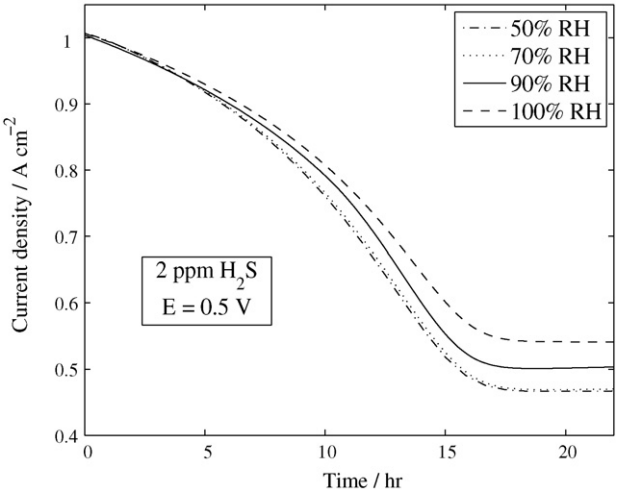

Fig. 12. The effect of channel water activity on H_2S poisoning for an H_2S concentration of 2 ppm and a cell voltage of 0.5 V. See Tables 4–10 for values of the other parameters.

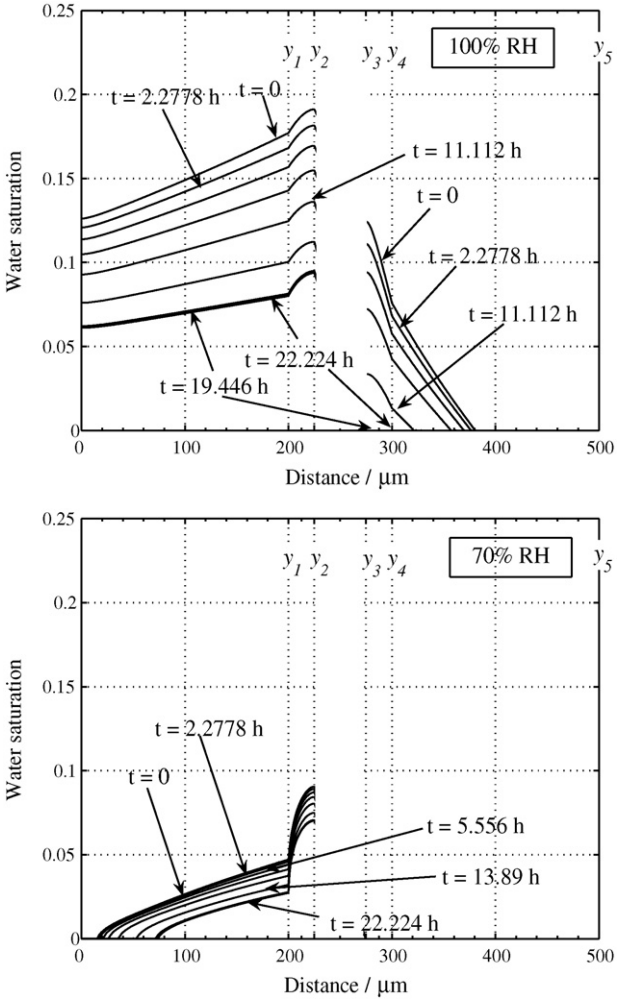

Fig. 13. The evolutions of the water saturation during the calculations at water activities of 1 and 0.7 shown in Fig. 12. See Tables 4–10 for values of the other parameters. The left-hand boundary, $y = 0$, corresponds to the cathode channel/gas diffusion layer interface and the right-hand boundary, $y = 500\,\mu m$, to the anode channel/gas diffusion layer interface. The region $225\,\mu m < y < 275\,\mu m$ corresponds to the membrane.

rate of water production and in the anode water is consumed in the oxidation reaction (R7). The lower current density will also reduce back diffusion caused by the drag of water molecules attached to protons, from the anode to cathode, as is seen from Eq. (6). A main consequence of the reduced saturation levels is a decrease in the membrane conductivity, which depends on the water content in the membrane according to Eq. (14). The water content in turn is a function of the local saturation and water vapour levels. Thus, the reduction in current density due to sulfur coverage of the platinum sites is compounded by a reduced membrane conductivity.

4. Conclusions

A modelling framework for predicting and studying the poisoning effect of H_2S on the anode catalyst layer of a PEM fuel cell has been developed. In contrast to the model in [16], the present model explicitly include mass, energy and momentum conservation, together with the fundamental modes of transport and a more detailed kinetic mechanism. The model can simulate both galvanostatic and potentiostatic operation. Comparison with data available in the open literature has shown that the trends are well captured

with respect to variations in the H_2S concentration, cell voltage and current.

The model predicts that temperature and water activity variations have a complicated effect on the poisoning process. The kinetic mechanism in the anode is intimately linked with variations in these quantities, which also yield a wider influence on performance, through the form of the reaction rates. For example, oxidation of sulfur from the platinum surfaces in the anode consumes water, and is therefore dependent on the channel water activity. It has been demonstrated that the anode water levels can decrease quite significantly as a consequence of this reaction. The decreased water levels in the anode will reduce the membrane conductivity, further decreasing the current density. The reduced current density as a result of poisoning in turn reduces the water production rate in the cathode and restricts back diffusion of water via proton migration. The relative strengths of these effects can be investigated with the model.

Temperature increases were shown in general to lessen the degree of poisoning, although the simulation results also suggest that the behaviour of the system over a relatively short timescale (before any steady state is reached) is not straightforward to predict and certain features may be masked by the steady-state results. For these relatively short timescales the results of this study agree with those of Mohtadi et al. [1], but at steady state the comparison is inconclusive. It has been hypothesised that the discrepancies found by Mohtadi et al. could be due to the relative changes in the rates of sulfur adsorption and oxidation as the operating temperature is varied. The adsorption rate almost certainly increases as the temperature is raised, but one can predict that there is a corresponding increase in the oxidation rate, which over long times could lead to better performance at higher temperature. More data is needed to verify these claims.

In this work several assumptions have been employed in relation to the kinetic model. The missing or estimated electrochemical constants can be estimated from experiment and input to the model, improving its accuracy. Future work will focus on obtaining these parameters and validating the model over a much broader range of operating conditions.

References

[1] R. Mohtadi, W.-K. Lee, J. van Zee, Appl. Catal. B 56 (2005) 37–42.
[2] S. Jiménez, J. Soler, R. Valenzuela, L. Daza, J. Power Sources 151 (2005) 69–73.
[3] T. Springer, T. Rockward, T. Zawodzinski, S. Gottesfeld, J. Electrochem. Soc. 148 (1) (2001) A11–A23.
[4] T. Loučka, J. Electroanal. Chem. 31 (1971) 319–332.
[5] X. Cheng, Z. Shi, N. Glass, L. Zhang, J. Zhang, D. Song, Z.-S. Liu, H. Wang, J. Shen, J. Power Sources 165 (2007) 739–756.
[6] J.J. Baschuk, X. Li, Int. J. Energy Res. 25 (2001) 695–713.
[7] K. Bhatia, C.-Y. Wang, Electrochim. Acta 49 (2004) 2333–2341.
[8] T. Loučka, J. Electroanal. Chem. 36 (1972) 369–381.
[9] T. Loučka, J. Electroanal. Chem. 44 (1973) 227.
[10] A. Contractor, H. Lal, J. Electroanal. Chem. 96 (1979) 175–181.
[11] R. Jayaram, A. Contractor, H. Lal, J. Electroanal. Chem. 87 (1978) 225–237.
[12] M. Mathieu, M. Primet, Appl. Catal. 9 (1984) 361–370.
[13] R. Mohtadi, W. Lee, S. Cowan, J. van Zee, M. Murthy, Electrochem. Solid State Lett. 6 (12) (2003) A272–A274.
[14] E. Najdeker, E. Bishop, J. Electroanal. Chem. 41 (1973) 79–87.
[15] W. Shi, B. Yi, M. Houa, F. Jing, P. Ming, J. Power Sources 165 (2007) 814–818.
[16] Z. Shi, D. Song, J. Zhang, Z.-S. Liu, S. Knights, R. Vohra, N. Jia, D. Harvey, J. Electrochem. Soc. 154 (7) (2007) B609–B615.
[17] F. Uribe, T. Zawodzinski, S. Gottesfeld, The Electrochemical Society and the International Society of Electrochemistry Meeting Abstracts, San Francisco, CA, 2–7 September, 2001.
[18] Y. Wang, H. Yan, E. Wang, J. Electroanal. Chem. 497 (2001) 163–167.
[19] C.-Y. Wang, Chem. Rev. 104 (2004) 4727–4766.
[20] A. Weber, J. Newman, Chem. Rev. 104 (2004) 4679–4726.
[21] C.-Y. Wang, P. Cheng, J. Power Sources 30 (1997) 93–196.
[22] C. Ziegler, H. Yu, J. Schumacher, J. Electrochem. Soc. 152 (8) (2005) A1555–A1567.
[23] A. Shah, G. Kim, P. Sui, D. Harvey, J. Power Sources 163 (2007) 793–806.
[24] A. Shah, P. Sui, G. Kim, S. Ye, J. Power Sources 166 (2007) 1–21.
[25] W. He, J. Yi, T. Nguyen, AIChE J. 46 (10) (2000) 2053–2064.
[26] S. Mazumder, J. Cole, J. Electrochem. Soc. 150 (11) (2004) A1510–A1517.
[27] D. Natarajan, T. Nguyen, J. Electrochem. Soc. 148 (12) (2001) A1324–1335.
[28] Y. Wang, C.-Y. Wang, Electrochim. Acta 50 (2005) 1307–1315.
[29] B. Bird, W. Stewart, E. Lightfoot, Transport Phenomena, John Wiley and Sons, 2002.
[30] S. Motupally, A. Becker, J. Weidner, J. Electrochem. Soc. 147 (9) (2000) A3171–A3177.
[31] Z. Wang, C.-Y. Wang, K. Chen, J. Power Sources 94 (2001) 40–50.
[32] T.E. Springer, T.A. Zawodzinski, S. Gottesfeld, J. Electrochem. Soc. 138 (8) (1991) A2334–A2341.
[33] J. Hinatsu, M. Mizuhata, H. Takenaka, J. Electrochem. Soc. 141 (1994) A1493–A1497.
[34] S. Ge, X. Li, B. Yi, I. Hsing, J. Electrochem. Soc. 152 (6) (2005) A1149–A1157.
[35] C. Berger, Handbook of Fuel Cell Technology, Prentice-Hall, Englewood Cliffs, NJ, 1968.
[36] J. Zhang, H. Wang, D.P. Wilkinson, D. Song, J. Shen, Z. Liu, J. Power Sources 147 (2006) 58–71.
[37] A. Adamson, Physical Chemistry of Surfaces, Interscience, New York, 1967.
[38] E. Gileadi, E. Kirowa-Eisner, J. Penciner, Interfacial Electrochemistry: An Experimental Approach, Addison-Wesley Publishing Company, Reading, MA, 1975.
[39] M. Mathias, J. Roth, J. Fleming, W. Lehnert, H.G.W. Vielstich, A. Lamm, in: Handbook of Fuel Cells—Fundamentals, Technology and Applications, vol. 3, John Wiley & Sons, Ltd., 2003 (Ch. 46).
[40] S. Lister, G. McLean, J. Power Sources 130 (2004) 61–76.
[41] M. Williams, H. Kunz, J. Fenton, J. Electrochem. Soc. 151 (10) (2004) A1617–A1627.
[42] T.V. Nguyen, W. He, W. Vielstich, A. Lamm, H. Gasteiger, in: Handbook of Fuel Cells—Fundamentals, Technology and Applications, vol. 3, John Wiley & Sons, 2003 (Ch. 46).
[43] U. Pasaogullari, C.-Y. Wang, K. Chen, J. Electrochem. Soc. 152 (8) (2005) A1574–A1582.
[44] J.J. Baschuk, X. Li, Int. J. Energy Res. 27 (2003) 1095–1116.
[45] Z. Ogumi, Z. Takehara, S. Yoshizawa, J. Electrochem. Soc. 131 (4) (1984) A769–A772.
[46] C. Wilke, P. Chang, AIChE J. 1 (2) (1955) 264–270.
[47] S.W. Cha, Scaling effects of flow channels in fuel cells, Ph.D. thesis, Stanford University, 2003.
[48] S. Um, C.-Y. Wang, K.S. Chen, J. Electrochem. Soc. 147 (12) (2000) A4485–4493.
[49] N. Siegel, M. Ellis, D. Nelson, M. von Spakovsky, J. Power Sources 115 (2003) 81–89.
[50] C. Ziegler, A. Schmitz, M. Tranitz, E. Fontes, J. Schumacher, J. Electrochem. Soc. 151 (12) (2004) A2028–A2041.
[51] M. Lampinen, M. Fomino, J. Electrochem. Soc. 140 (12) (1993) A3537–A3546.